JOURNAL OF GEOPHYSICAL RESEARCH, VOL. 117, B11307, doi:10.1029/2012JB009550, 2012

Microseisms and hum from ocean surface gravity waves

James Traer,[1] Peter Gerstoft,[1] Peter D. Bromirski,[1] and Peter M. Shearer[1]

Received 19 June 2012; revised 28 September 2012; accepted 4 October 2012; published 28 November 2012.

[1] Ocean waves incident on coasts generate seismic surface waves in three frequency bands via three pathways: direct pressure on the seafloor (primary microseisms, PM), standing waves from interaction of incident and reflected waves (double-frequency microseisms, DF), and swell-transformed infragravity wave interactions (the Earth's seismic hum). Beamforming of USArray seismic data shows that the source azimuths of the generation regions of hum, PM and DF microseisms vary seasonally, consistent with hemispheric storm patterns. The correlation of beam power with wave height over all azimuths is highest in near-coastal waters. Seismic signals generated by waves from Hurricane Irene and from a storm in the Southern Ocean have good spatial and temporal correlation with nearshore wave height and peak period for all three wave-induced seismic signals, suggesting that ocean waves in shallow water commonly excite hum (via infragravity waves), PM, and DF microseisms concurrently.

Citation: Traer, J., P. Gerstoft, P. D. Bromirski, and P. M. Shearer (2012), Microseisms and hum from ocean surface gravity waves, *J. Geophys. Res.*, *117*, B11307, doi:10.1029/2012JB009550.

1. Introduction

[2] Microseisms, low amplitude wave-induced signals that are ubiquitous in seismic recordings, have long been regarded as a nuisance in the study of transient seismic signals, such as earthquakes and active sources. However, recent advances in array processing tomography using diffuse ambient noise have resulted in a resurgence of interest in microseisms and their generation [*Bromirski*, 2001; *Bromirski et al.* 2005; *Chevrot et al.*, 2007; *Kedar et al.*, 2008; *Gerstoft et al.*, 2008; *Ardhuin et al.*, 2011; *Kedar*, 2011; *Ardhuin et al.*, 2012; *Hillers et al.*, 2012]. The noise correlations, used in the tomographic inversions, are affected by the distribution of noise sources [*Weaver et al.*, 2009; *Harmon et al.*, 2010; *Froment et al.*, 2010]. A greater understanding of the generation mechanisms and regions of microseismic noise will allow the noise distributions to be better estimated, facilitating more accurate inversions. Here we correlate the microseismic and hum noise with global ocean wave measurements to better localize their source. We consider different generation mechanisms of microseisms and the Earth's seismic hum, all of which result from ocean wave activity, and are thus closely linked.

[3] The term microseism refers to ocean-wave generated seismic signals in two frequency bands, that of ocean gravity waves (0.04–0.17 Hz), known as primary microseisms (PM), and a higher frequency band at twice the ocean wave frequency (0.08–0.34 Hz), known as double-frequency (DF) microseisms. The bands overlap due to the broad frequency range of ocean wave energy. It is well established that DF signals can be generated by the interaction of opposing waves, and the resulting pressure excitation pulse propagates energy to the seafloor in deep water [*Longuet-Higgins*, 1950; *Hasselmann*, 1963]. A depth-dependent resonance suggests certain areas of the ocean are more conducive to DF microseism generation than others [*Longuet-Higgins*, 1950; *Kedar et al.*, 2008]. The opposing wavefields may be generated by opposing winds, multiple storm systems, or by reflection of waves off coastlines. Because the gravity wave pressure signal decays exponentially from the sea surface, PM microseisms are generated only in shallow coastal waters.

[4] Efficient coupling of microseism energy to propagating seismic modes requires that the water column pressure waves at the seafloor, match phase speeds with the seismic waves [*Hasselmann*, 1963]. Thus the seafloor transfer function depends on the seafloor composition, topography and layered structure. This transfer function is poorly known, but some regions of the ocean might be active sources of microseisms when illuminated by ocean waves with certain spectral properties. Some regions may excite microseismic body waves, others microseismic surface waves, or both.

[5] Much work has been done to identify the source regions of microseisms. Microseism power fluctuations have been correlated with wave buoy data [*Bromirski et al.*, 1999] and seafloor hydrophones [*Duennebier et al.*, 2012]. Beamforming with seismic arrays can estimate the incidence direction of microseismic noise. When applied to body waves, this identifies the region of microseism generation [*Gerstoft et al.*, 2008; *Landès et al.*, 2010; *Zhang et al.*, 2010]. These studies indicate that mid-ocean storms generate microseism P-waves, and the source regions vary seasonally with the predominant waves. Beamforming of surface waves [*Gerstoft and Tanimoto*, 2007], or correlating horizontal and vertical oscillation components [*Stutzmann et al.*, 2009; *Kedar et al.*, 2008; *Schimmel et al.*, 2011], identifies the incident azimuth of

---

[1] Scripps Institution of Oceanography, University of California, San Diego, La Jolla, California, USA.

Corresponding author: J. Traer, Scripps Institution of Oceanography, University of California, San Diego, 9500 Gilman Dr., La Jolla, CA 92093, USA. (jtraer@ucsd.edu)

0148-0227/12/2012JB009550

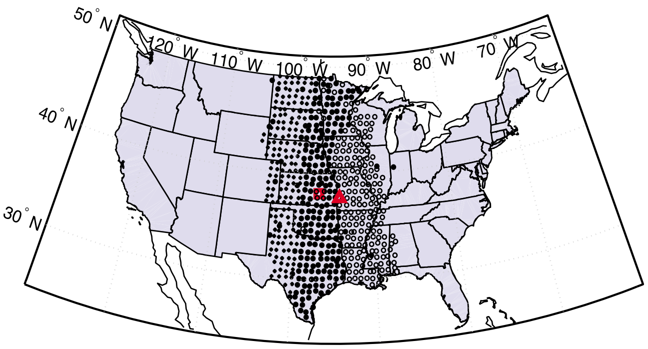

Figure 1. The locations of the stations used in beamforming (asterisks) Sep–Dec and (open circles) Jan–Aug and the array centers (square and triangle).

microseismic surface waves, but back-propagating along these azimuths intersects large swaths of ocean. Rayleigh wave microseism signals, which are the most energetic microseism signals detected on land, correlate best with waves in coastal regions [*Bromirski*, 2001; *Chevrot et al.*, 2007].

[6] Global double-frequency pressure excitation estimates (Ψ from *Kedar et al.* [2008]) have been computed from measurements and model hindcasts of gravity wave directional spectra. Taking into account acoustic resonances from the ocean depth, a model of double-frequency pressure oscillations at the seafloor Ψ_c can be computed [*Kedar et al.*, 2008]. A comparison of this source distribution with beamforms of microseismic P-waves suggests that the model qualitatively agrees with deep ocean observations but underestimates coastal microseism generation [*Hillers et al.*, 2012]. An improved double-frequency pressure excitation model, including wave reflections from both coasts and icebergs, was presented by *Ardhuin et al.* [2011]. These models indicate likely source regions of DF microseisms but do not consider PM microseisms or hum.

[7] The Earth's hum, a low-amplitude low-frequency signal (0.002–0.03 Hz, with power 300 times smaller than that of DF microseisms [*Webb*, 2008]), has been the subject of much recent research [*Nishida and Kobayashi*, 1999; *Nishida et al.* 2000; *Ekström.*, 2001; *Rhie and Romanowicz*, 2004, 2006; *Webb*, 2007; *Tanimoto*, 2008; *Uchiyama and McWilliams*, 2008; *Webb*, 2008; *Bromirski and Gerstoft*, 2009]. Theoretical work suggests that infragravity waves, with frequencies of 0.1–20 mHz and wavelengths on the order of 10's of kilometers [*Holman and Bowen*, 1984], generate the hum signal [*Tanimoto*, 2008; *Uchiyama and McWilliams*, 2008; *Webb*, 2008; *Fukao et al.*, 2010]. The hum signal is low enough in frequency that hum Rayleigh waves circle the globe, exciting oscillation of the Earth's normal modes [*Webb*, 2008]. Due to the large propagation distances of hum signals and their ubiquitous presence, they might provide an ideal source-signal for seismic tomography [*Nishida et al.*, 2009].

[8] Infragravity waves, a family of low-frequency gravity waves, result from the nonlinear transformation of ocean swell interacting with the nearshore seafloor [*Guza and Davis*, 1974; *Holman and Bowen*, 1984; *Herbers et al.*,1995; *Lippmann et al.*, 1997; *McWilliams et al.*, 2004; *Thomson et al.*, 2006, *Svendsen*, 2006]. Most of the energy contained in infragravity waves remains refractively trapped along coastlines [*Herbers et al.*, 1995; *Thomson et al.*, 2005] although some infragravity wave energy, known as "leaky modes," become free waves and propagate across ocean basins [*Bromirski et al.*, 2010]. Due to their long wavelengths, infragravity waves cause pressure oscillations on the deep ocean seafloor. Thus infragravity waves can generate hum either by direct interaction with the seafloor, analogous to PM, or by opposing infragravity wave interactions, analogous to DF signals. In this study we do not distinguish between hum from direct and double-frequency infragravity wave interactions.

[9] Infragravity waves are important for coastal sediment transport and potentially play a role in the fracturing of Antarctic ice shelves [*Bromirski et al.*, 2010; *Bromirski and Stephen*, 2012]. However, as they are low-amplitude compared to the swell waves (on the order of 10 cm), they are difficult to measure remotely and most infragravity wave observations are made with pressure sensors for short duration experiments. However, localization of hum signal generation regions may provide a proxy for the global spatial and temporal variability of infragravity waves. Infragravity waves continually interact with the seafloor [*Crawford et al.*, 1991], however, they are generated nearshore and most infragravity wave energy remains refractively trapped along coastlines. Infragravity wave energy and associated hum excitation are therefore expected to be greatest in coastal waters.

[10] Recent attempts to locate dominant hum source areas (and therefore infragravity wave generation regions) suggest that most hum signals are generated in coastal waters, especially the west coasts of North America, Mexico and Europe [*Rhie and Romanowicz*, 2006; *Webb*, 2008; *Bromirski and Gerstoft*, 2009]. These locations are, in part, due to west-to-east storm propagation. This causes more long period swell energy to impact these regions, which is then transformed to infragravity waves at the respective coasts.

[11] We compare the ambient seismic noise variability with modeled global significant wave height to infer the dominant wave-induced seismic signal generation regions. We use both beamforming and correlation with ocean wave height and we apply the same technique to hum, PM and DF frequency bands. The direction of incidence of seismic noise is computed with broadband seismometer data collected by the USArray over a year. The data are filtered to isolate frequency bands associated with hum, PM and DF microseisms. The beamformer outputs are compared with wave heights and peak periods from National Oceanic and Atmospheric Administration (NOAA) hindcasts [*Tolman*, 2005]. Likely oceanic generation regions of signals in the three seismic bands are identified by correlation of time series of significant height wave at each grid point with the beamformer output. Waves generated by Hurricane Irene impacting the east coast of North America and waves from a storm in the Southern Ocean impacting the west coast of North America are examined in detail. We assume that regions of high correlation are regions of the ocean in which the seafloor depth and structure, and the predominant directional surface-wave spectrum, are conducive for generation of microseism and hum Rayleigh waves.

2. Overview of Data and Processing

2.1. Seismic Data

[12] One year of continuous vertical-motion seismic data from a 425-station subset of the USArray, from September

Table 1. Frequency and Slowness Bands Processed for One Year of Data (Section 3), and for 11 Days of Data (Aug. 23–Sep. 4, 2011) to Isolate Signal From Hurricane Irene (Section 4) and Swell Incident on the Pacific Coast of North America (Section 5)

	Hum/IG	PM	DF I
	One Year		
Passband (mHz)	5–20	60–85	110–130
Passband (s)	200–50	11.7–16.6	10–7.14
Slowness band (s/km)	0.23–0.27	0.28–0.32	0.29–0.33
	Hurricane Irene		
Passband (mHz)	5–20	60–130	160–260
Passband (s)	200–50	16.67–7.69	6.25–3.85
Slowness band (s/km)	0.04–0.4	0.04–0.4	0.04–0.4
	Pacific Swell		
Passband (mHz)	5–20	30–80	80–160
Passband (s)	50–200	12.5–33.33	12.5–5.26
Slowness band (s/km)	0.04–0.4	0.04–0.4	0.04–0.4

2010 through August 2011, was processed as described below. The locations of the stations used are shown in Figure 1. Some of the stations moved during the deployment. However, the change in the array center throughout the time period evaluated was small relative to the scale of the wavefronts considered. Thus, the change in array configuration does not have a significant effect on the beamformer output. The large number of stations distributed in a horizontal plane gives azimuthal resolution of less than 1° over all the frequencies associated with the seismic surface waves studied.

[13] Processing was repeated for three frequency bands (Table 1). The lowest frequency band (0.005–0.02 Hz or 200–50 s period) corresponds to the higher frequency range of infragravity waves and the Earth's seismic hum. Although infragravity waves exist at lower frequencies we exclude such low frequencies to eliminate contributions from tidal pressure signals. The second band (0.05–0.08 Hz or 20–12.5 s period) corresponds to PM from long period ocean waves. Primary microseisms are likely to be generated waves with frequencies higher than 0.08 Hz, but DF interactions of low-frequency components might also be generated in these bands. Thus the PM results presented here are limited to long-period ocean waves. The third band (0.11–0.13 Hz or 10–7.4 s) contains the peak of the DF spectrum. As DF energy levels are much larger than PM energy, this band is dominated by DF signals. Short-period waves might generate PM at these frequencies, but these PM contributions are likely much less energetic than DF signals in this band.

[14] Microseism signals are many orders of magnitudes smaller in amplitude than modest sized earthquakes, which occur many times on any given day. In order to use an entire year of data, without contamination from earthquakes, we truncate extreme values in the raw data and apply smoothing and amplitude normalization. As we assume a stochastic model of coupling between surface waves and microseisms, averaging over long timescales is necessary to provide ensemble averages (section 2.3).

[15] The processing can be summarized as: (1) Passband filter the data, to isolate signals from hum, PM and DF contributions (see Table 1). (2) Truncate to remove contamination from earthquakes. (3) Fourier transform in sequential time windows. (4) Normalize such that each frequency bin has an amplitude of 1, and only the phase information is retained. (5) Beamforming: The normalized frequency domain representations were summed with specific phase delays to sum contributions from specific azimuths and slownesses in phase. (6) Average over slowness and frequency bands (see Table 1). (7) Truncate extreme values to remove transient peaks. (8) Smooth over time. (9) Normalize such that each monthly beamformer output has a maximum value of one. (10) Interpolate the beamformer output to form a time series corresponding to the azimuth connecting the center of the array to each hindcast grid point. (11) Smooth the hindcast time series over space and normalize each monthly time series to have a maximum value of one. (12) Cross-correlate the normalized monthly beamformer output with the normalized monthly hindcast to give the *correlation of beamformer output and hindcast* (CBH). Each step is described in detail and justified in section A1.

[16] The beamformer output was consistently dominated by contributions from slownesses associated with Rayleigh waves. Although we have not quantitatively accounted for the geometric array gain response this is consistent with prior work that suggests Rayleighwaves microseisms contain more energy than body waves [*LaCoss et al.*, 1969]. As such we have restricted the following analysis to Rayleigh wave slownesses only. Similar beamforming techniques with different arrays have been applied to body waves [*Landès et al.*, 2010; *Hillers et al.*, 2012].

2.2. Ocean Wave Hindcasts

[17] The NOAA ocean wave hindcasts use assimilated surface buoy measurements, and the physics of ocean wave propagation [*Tolman*, 2005] to compute significant wave height and peak period. They are sampled every 3 h, on a 0.5°-spaced grid from 77.5°S to 77.5°N and 0–365.5°E. The hindcasts are good proxies for the total surface wave energy, but not necessarily for microseism source regions, which will depend upon the directional spectral distribution of wave energy and the seafloor structure, as discussed in section 2.3.

[18] It is well established that microseism signals are generated by ocean waves. Robust models of ocean waves have been developed that generate wave directional spectra to estimate opposing gravity wave components, which are required for the generation of DF microseims [*Kedar et al.*, 2008; *Ardhuin et al.*, 2011]. Here, we assume that the microseism energy generated at a given point in the ocean is a stochastic variable with an expected value that scales with significant wave height (equation (2)). Thus although the seafloor transfer function and spectral distribution are unknown, averaging over sufficiently long time periods, that span several synoptic storm occurrences, yields a satisfactory estimate of the expected microseism contribution in a particular region.

2.3. Significant Wave Height and Seismic Signals

[19] In this work we examine hum and PM microseisms, as well as DF microseisms. DF estimates from wave models are poor proxies of source regions for hum and PM as these signals are generated by wave energy through different pathways. The PM signals result from the direct interaction of wave-induced pressure on the seafloor. Hum generation requires the transformation of ocean surface gravity waves along coastlines into infragravity waves.

[20] All of the gravity-wave induced seismic signal-generation pathways depend on the local seafloor structure and the 2D directional spectra of incident waves, such that the directional microseism spectrum $M(f, \theta, \phi, \mathbf{x}, t)$ is given by

$$M(f,\theta,\phi,\mathbf{x},t) = H_{f,\mathbf{x}}[F(f,\theta,\mathbf{x},t)], \tag{1}$$

where $H_{\mathbf{f},\mathbf{x}}$ is the transfer function of the ocean and seafloor at frequency f, location $\mathbf{x}$, and time t. $F(f, \theta, \mathbf{x}, t)$ is the directional wave spectrum [*Hasselmann*, 1963; *Ardhuin et al.*, 2011]. Note that the microseismic spectrum is 3D and varies with azimuth θ and the angle between the propagation direction and the Earth's surface ϕ (equivalent to slowness), while the surface wave spectrum is 2D and varies only with θ. $H_{f,\mathbf{x}}$ has been computed for horizontally homogenous half-spaces [*Hasselmann*, 1963] but, in general, it is unknown. It depends on ocean depth and crustal structure. In the following equations we drop the explicit mention of $\mathbf{x}$ and t where possible.

[21] We consider an alternative transfer function

$$\begin{aligned} \mathrm{E}\{M(f,\theta,\phi)\} &= H_f[E(f)\mathrm{E}\{M(\theta)\}] \\ &= G_f[E(f)] \\ F(f,\theta) = E(f)M(\theta), & \int_0^{2\pi} M(\theta)\mathrm{d}\theta = 1, \end{aligned} \tag{2}$$

where, following the model of *Ardhuin et al.* [2011], the surface-wave spectra are described by frequency $E(f)$ and normalized directional $M(\theta)$ components. The expected value of $M(\theta)$, denoted by $\mathrm{E}\{M(\theta)\}$, is determined by the prevailing winds and geographic location. For example, near a coastline, $M(\theta)$ is likely dominated by wave energy incident from seaward directions, where the fetch is large. A small contribution of energy reflected from the coast depends on coastline configuration relative to the incident wave energy, as well as nearshore slope steepness and beach composition. $G_{f,\mathbf{x}}$ is the location dependent transfer function which incorporates both the seafloor properties and $\mathrm{E}\{M(\theta)\}$ at point $\mathbf{x}$. As $\mathrm{E}\{M(\theta)\}$ is an ensemble average, equation (2) is only true if a similar ensemble average is obtained from the measured microseism signal.

[22] Integrating over the frequencies within each frequency band, and considering only the microseisms propagating with directions that impinge upon the array, three transfer functions can be estimated from

$$\begin{aligned} \mathrm{E}\{M_{\mathrm{hum}}\} &= \tilde{G}_{\mathbf{x}}^{(\mathrm{hum})}\left[\int_{\mathrm{hum}} E(f)\mathrm{d}f\right] \approx \alpha_{\mathrm{hum}}\tilde{G}_{\mathbf{x}}^{(\mathrm{hum})}[S_{\mathbf{x}}] \\ \mathrm{E}\{M_{\mathrm{PM}}\} &= \tilde{G}_{\mathbf{x}}^{(\mathrm{PM})}\left[\int_{\mathrm{PM}} E(f)\mathrm{d}f\right] \approx \alpha_{\mathrm{PM}}\tilde{G}_{\mathbf{x}}^{(\mathrm{PM})}[S_{\mathbf{x}}] \\ \mathrm{E}\{M_{\mathrm{DF}}\} &= \tilde{G}_{\mathbf{x}}^{(\mathrm{DF})}\left[\int_{\mathrm{DF}} E(f)\mathrm{d}f\right] \approx \alpha_{\mathrm{DF}}\tilde{G}_{\mathbf{x}}^{(\mathrm{DF})}[S_{\mathbf{x}}] \quad , \end{aligned} \tag{3}$$

where $\tilde{}$ indicates that we consider only the values of θ and ϕ that intersect the USArray, and, on the RHS, we have made the assumption that $\int_\Omega E(f)\mathrm{d}f$ is proportional to the significant wave height $S_{\mathbf{x}}$, for $\Omega = \{\mathrm{hum, PM, DF}\}$. α_Ω is an unknown constant.

[23] We correlate global measurements of significant wave height $S_{\mathbf{x}}$, with measured microseism Rayleigh waves traversing the USArray. The results presented here, therefore, show estimates of the relative values of the transfer function $\tilde{G}_{\mathbf{x}}$ for hum, PM and DF microseisms (equation (3)). These are the regions of the Earth's oceans in which the large waves are likely to produce, through complex interactions with the seafloor and coasts, the appropriate gravity wave conditions for hum, PM or DF microseism Rayleigh waves. Previous studies suggest that there is a strong correlation between significant wave height and local microseisms [see *Bromirski et al.*, 1999, Figure 3].

3. One Year of Data

3.1. Beamformer Output

[24] In the 0.005–0.02 Hz band associated with seismic hum and infragravity waves, the beamformer output Figure 2 shows dominant signals incident from 150–220°, especially in the SH winter. The great circle paths from these azimuths transect the South Pacific and the Gulf of Mexico, intersecting the coasts of Central and South America and Antarctica (Figures 2b and 2c). In the NH winter, signals are observed from 50–65° and 285–330°, which transect the North Atlantic and North Pacific, intersecting the coasts of Greenland, Europe, Alaska, Kamchatka and Japan (Figure 2c).

[25] In the 0.06–0.08 Hz band associated with PM from long period ocean waves, the beamformer output Figure 2d shows the highest amplitude signals incident from 20–55°, consistent with generation in the North Atlantic (Figures 2e and 2f). These peaks are strongest in the NH winter, but remain strong through the SH winter. Several peaks of seismic energy are recorded in a similar time period from 295–330° (Figure 2d), consistent with generation in the North Pacific. A signal is detected from 345–355° whose origin is not clear. These azimuths intersect the Arctic ocean, which is covered in ice during the NH winter, although 2010 had less ice coverage in the arctic than average years [*Stroeve et al.*, 2011]. During the SH winter the dominant signal is from 220–240°, consistent with signals from the coast of Mexico, the South Pacific and New Zealand (Figure 2e).

[26] In the 0.11–0.13 Hz band associated with DF microseisms, the peak microseismic signals are incident from 30–70°, 170–220° and 240–310° (Figure 2g). The signals from 170–240° are dominant in the SH winter and correspond to great circle paths that transect the South Pacific intersecting the coasts of Mexico, Antarctica, New Zealand and Australia (Figure 2h). The other azimuths are prominent in the NH winter and transect the North Atlantic and North and South Pacific (Figure 2i). The paths that intersects the Pacific coast of Mexico and the coasts of Australia and Antarctica show strong microseism signals throughout both the SH and NH winters.

[27] The beamformer output in all three bands is dominated by a few azimuths with strong signals, which suggests certain regions consistently excite seismic waves. Both the hum and PM bands show strong signals from 20–60° and 280–330°, both of which intersect long stretches of coastal areas (Figure 2). This is not surprising because PM microseisms can only be generated in shallow water [*Hasselmann*, 1963] and high-amplitude infragravity waves are only generated in coastal regions [*Herbers et al.*, 1995]. The DF beamformer output shows signal from 30–60° (N. Atlantic), consistent with the PM and hum signals, but not 280–330° (N. Pacific), in contrast with the PM and hum signals.

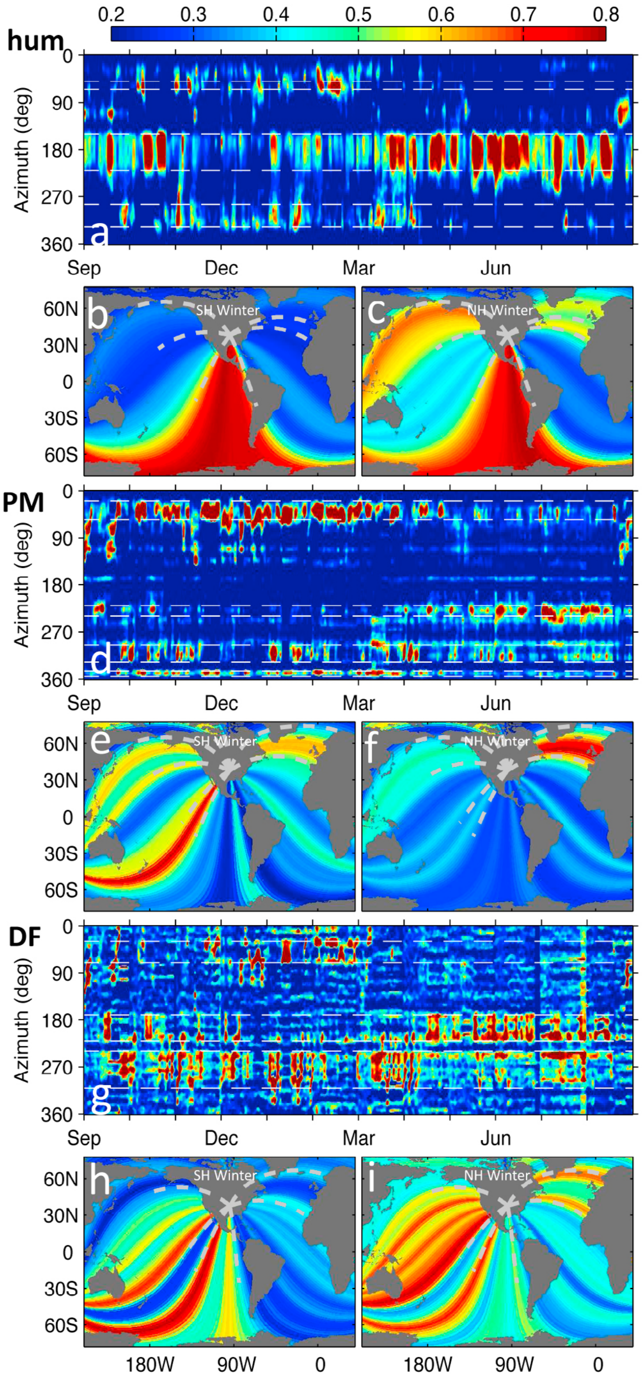

Figure 2. The normalized beamform power response from Sep 2010–Aug 2011 averaged over the frequency and slowness bands given in Table 1 for (a) hum, (d) PM and (g) DF. The beam power averaged over the SH (Figures 2b, 2e, and 2h) and NH (Figures 2d, 2f, and 2i) winter are normalized and plotted along the great circle paths associated with their direction of incidence for (b and c) hum, (e and f) PM and (h and i) DF. The great circle paths marked on the maps are plotted on the beamformer output.

However, in the SH winter the dominant hum signal is incident from a large azimuth range from 160–210°, while the dominant PM signal is incident from a narrow beam at 220–240°. Thus while both hum and PM are expected to be generated in coastal waters their regions of dominant generation may be different coasts.

[28] The DF beamformer output contains strong signals from 30–70°, but otherwise detects signals from slightly different azimuths than hum and PM. The azimuths of strong DF signals transect the mid-North Pacific, rather than its northern coasts, as do the azimuths of strong PM and hum. This difference might result from deep water DF generation in the Pacific or from wave interactions along different coastlines that do not produce dominant PM or hum.

3.2. Ocean Wave Hindcasts

[29] Ocean wave heights are large in the Southern Ocean throughout the year (Figure 3a and 3b). In the NH winter, large waves are also observed in the North Atlantic and North Pacific (Figure 3b). Summing the contributions along great circle paths shows the distribution of ocean wave energy with azimuth from the center of the USArray (Figures 3c and 3d). Summing over the global ocean hindcast grid identifies dominant wave energy from 220°, which corresponds to a path transecting the Southern Ocean south of New Zealand and Australia. Azimuths that transect the South Atlantic and intersect the Southern Ocean south of Africa also detect high amplitude waves (Figure 3c). Azimuths that transect the far Northern regions of the Atlantic and Pacific Oceans show strong signal in the NH winters (Figure 3d).

[30] Summing over only contributions within 500 km of the coastline gives a much stronger preference to the signals from the northern regions of the Atlantic and Pacific Oceans, as the great circle paths that transect these areas intersect many coastlines. A strong signal is observed at 160° which passes parallel to the Pacific coasts of Central and South America (Figure 3d). Strong signals are observed at 50° and 315° consistent with regions of strong PM and hum signal (Figure 2).

[31] The generation mechanism for both infragravity waves and PM microseisms requires that the ocean surface-waves to interact with the seafloor. For a 60 mHz ocean gravity wave (about an 18 s period swell), which we consider a representative swell frequency that generates PM signals (see Table 1), the wavelength is 434 m. Significant interactions of gravity waves with the seafloor begin to occur at water depths of 1/2 their wavelength, λ [*Bromirski and Duennebier*, 2002] (see section 2.3). Such water depths are generally found only within a hundred kilometers of coastlines. We use the term "coastal water" to refer to areas within 100 km of coastlines. While these regions include water deeper than λ / 2, similar significant wave heights and peak periods to nearby shallow water regions will occur, as these wave parameters are well correlated over relatively large spatial scales (Figure 3) [*Bromirski et al.*, 1999].

3.3. Correlation of Beamformer Output and Ocean Waves

[32] Beamforming alone is not sufficient to localize the region of microseism and hum generation, as the great circle paths extending from the array center along a given azimuth transect a large region of ocean and potentially multiple coastal zones (Figure 2). The average beamform power distribution versus azimuth differs substantially from the globally integrated wave height (Figure 3c) for all frequency bands. This is not surprising, because the microseisms are

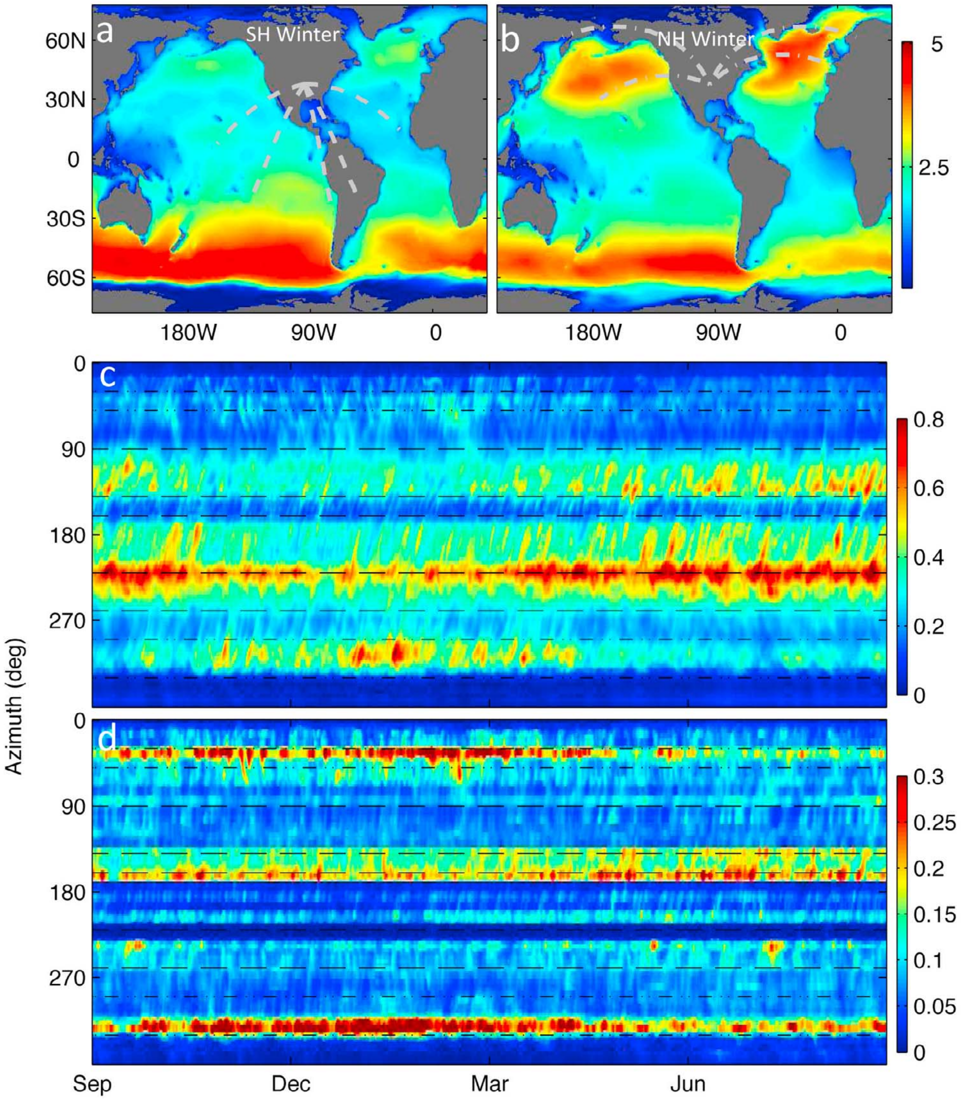

Figure 3. The mean significant wave height from Sep 2010–Aug 2011 for the (a) SH and (b) NH winter. The sum of the wave heights intersected by each azimuth (Figure 2) for (c) the global ocean and (d) areas within 500 km of the coasts. Dashed and dash-dotted lines emanating from the array center in Figures 3a and 3b show azimuths plotted in Figures 3c and 3d.

not generated simply by large waves; they require either shallow water or opposing wave trains. Much better correlations can be obtained if the time dependence of the signals is considered. The hindcast data show that ocean surface gravity waves typically evolve over a scale of days (which is why the 3 h sampling is sufficient). Our USArray beamform observations show that Earth noise changes amplitude over similar timescales. Cross-correlation of the beamformer output and hindcast time series thus provides a way to link the two signals. We estimate the range along each azimuth at which the ocean wave energy couples into seismic waves by cross-correlating the significant wave height time series at each grid point of the wave model hindcasts with the beamformer time series at the azimuth intersecting the grid point.

[33] Deep-water surface gravity waves propagate at 10 m/s (13 s period) and thus take several days to cross the ocean basins. Seismic Rayleigh waves travel at 3.5 to 4 km/s and hence travel 180 degrees in about 1.5 hours. Thus, in the time the seismic waves propagate from the point of generation to the USArray, the change in the surface wavefield will be negligible, and we need only consider the zero-lag CBH. A similar approach with data from wave buoys was used by *Bromirski and Gerstoft* [2009] and *Ardhuin et al.* [2012]. Here we use the hindcast data to estimate the global CBH.

[34] As the great circle path associated with a given azimuth intersects many regions of ocean the CBH is subject to errors due to the coastal geometry and the angle of incidence of waves on the coast. This is discussed in section A3.

3.3.1. Hum and Infragravity Waves

[35] During the NH winter strong hum signals are observed from 280–320° consistent with seasonal waves in the North Pacific (Figures 2a and 4a). Large transient peaks are observed between 55–75°, consistent with seasonal waves in the North Atlantic (Figures 2a and 4a). The CBH gives its highest values near coasts, with the CBH in the Pacific peaking off the coasts of northwest Canada, Alaska

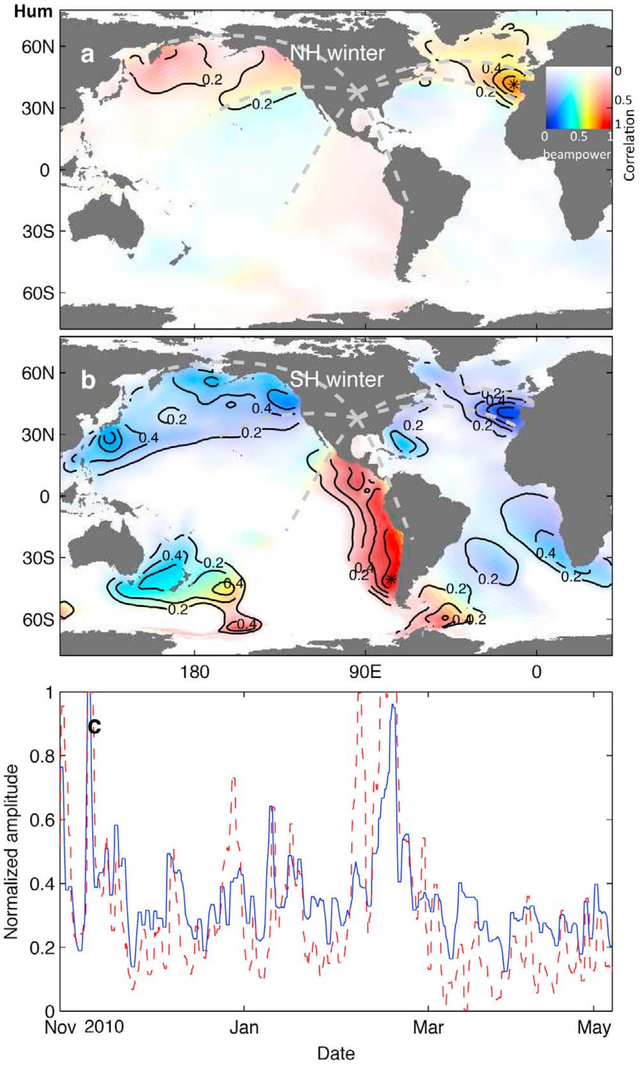

Figure 4. Hum correlations. The correlation of beamformer output and ocean wave hindcasts (CBH) for the (a) NH and (b) SH winters. Each point in the ocean is colored with hue varying with the normalized beam power incident from that direction over 6 months and intensity varying with the value of the normalized cross-correlation of the beamformer output with the ocean wave hindcast. The dashed lines correspond to the azimuths marked in Figures 2a–2c. Contours show the normalized cross-correlation. The maximum correlation for each 6-month period is marked (asterisks). (c) The beamformer output (dashed) from the azimuth of the great circle path to the maximum correlation for the NH winter, the asterisks in Figure 4b, and the significant wave height (solid) at this point. For the year, the correlation mean, maximum and standard deviation were: $\bar{c} = 5.4 \times 10^{-3}$, max($c$) = 5.3×10^{-2}, $\sigma_c = 7.9 \times 10^{-3}$.

and northeast Kamchatka. In the Atlantic, the highest CBH value observed globally is just off the west coast of the Iberian peninsula (Figure 4a).

[36] During the SH winter, the CBH is also highest near coasts, with peak values just off the coasts of Central and South America (Figure 4b). This is consistent with the large waves from the Southern Ocean illuminating the long coastline of the American continents and generating infragravity waves, in agreement with *Bromirski and Gerstoft* [2009].

[37] During the SH winter (Figure 4b), seismic surface wave hum signals also correlate with ocean waves off the coasts of Japan, Alaska, the Pacific coast of North America, the Atlantic coast of Europe, New Zealand and the Atlantic coast of southern Africa. However, the power incident from these directions is much smaller than that from the Pacific coast of Central and South America. In almost all cases, the CBH is highest near coastlines, indicating that storm waves produce maximal hum signals when waves impacted the coast, where they are transformed into infragravity waves. The New England coast of the United States gives higher CBH values than the mid Atlantic (Figure 4b), consistent with hum signals produced by the transformation of Hurricane Irene-generated waves propagating northward along this section of coast (section 4).

[38] The maximal CBH for the entire year of hum data occurred near the coast of Portugal (the asterisks in Figure 4a). The time series of the beamformer output from this azimuth and the model of significant wave height from this location show that large amplitude waves arriving at the Portuguese coast correlate well with transient spikes in the beamformer output (Figure 4c). The large February signal is consistent with the presence of large storms in the North Atlantic [*Hanafin et al.*, 2012]. However, the amplitudes are not comparable as the beamformer output is normalized.

[39] Note that the great circle path from the array intersects this coastline approximately perpendicularly. If infragravity waves and hum are predominantly generated in shallow near-coastal waters, we expect a good CBH from this geometry, as each point on the coast corresponds to a different azimuth determined by the beamformer. Thus a wave event that illuminates different stretches of coastline at different times is observed by the beamformer as a series of peaks at different azimuths and times. The peak at each azimuth will correlate with the wave peak and a good CBH results. In the case of a coastline parallel to the great circle path, as occurs for the Pacific coasts of South and North America, multiple regions of coastline may contribute at the same azimuth, and thus we expect a lower CBH value from these coasts. In this case a wave event that excites different stretches of coastline at different times will produce multiple peaks at the same azimuth, while the hindcasts contain an individual peak at each point along the coast. Thus the CBH along coastlines parallel to great circle paths from the array are likely to be underestimated, unless the coastline is illuminated by waves perpendicularly.

[40] For both the NH and SH winters, the highest CBH occurred near coastlines, often monotonically decreasing with distance from the coast. This is consistent with the generation of hum by waves impacting the coastlines. The CBH indicates that the largest hum signals are produced along the Pacific coasts of Central and South America in the SH winter, and along the coasts of Alaska, Kamchatka, and the Iberian peninsula in the NH winter.

3.3.2. Primary Microseisms

[41] During the NH winter the CBH in the PM frequency is highest near the southern tip of Greenland and the east coast of Newfoundland (Figure 5a). However, as there is no mechanism to generate signals at these frequencies except in

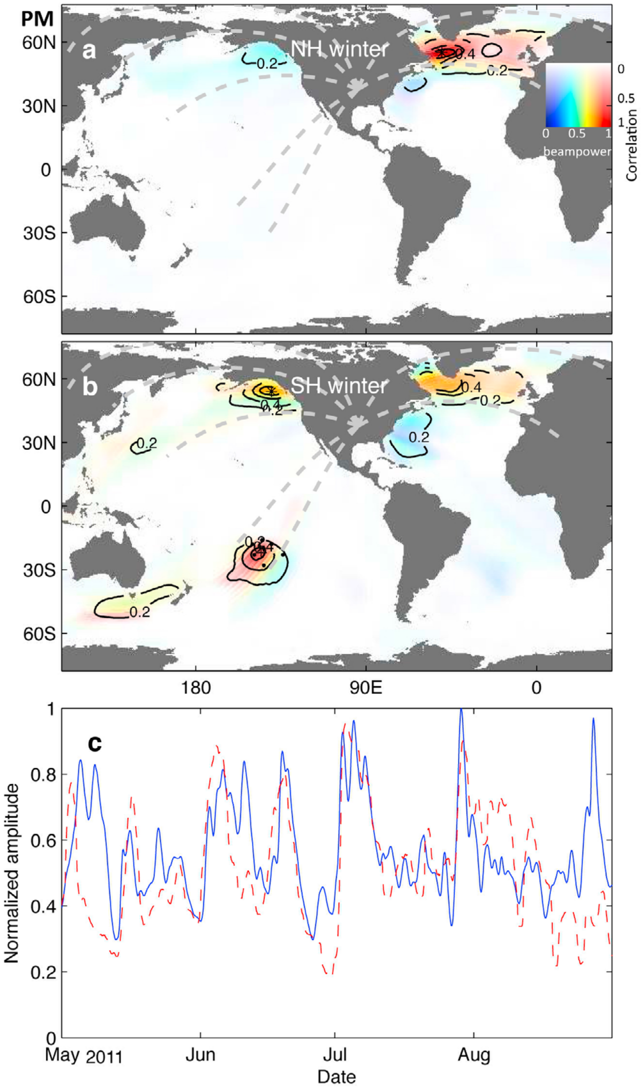

Figure 5. Primary microseism correlations. (a and b) The same as Figures 4a and 4b with a beamformer output averaged over 0.06–0.08 Hz and 0.28–0.32 s/km. The dashed lines correspond to the azimuths marked in Figures 2d–2f. (c) The time series from four months of the SH winter from the point in the South Pacific marked with a + in Figure 5b. The location of several islands in the Polynesian chain are shown with dots. For the year, the correlation mean, maximum and standard deviation were: $\bar{c} = 1.6 \times 10^{-3}$, $\max(c) = 4.6 \times 10^{-2}$, $\sigma_c = 4.7 \times 10^{-3}$.

very shallow water, this is likely due to the fact that ocean waves are well-correlated over large spatial scales [*Bromirski et al.*, 1999], which would smear the CBH in space and time. The signals are likely generated both on the coasts of Greenland and Newfoundland. Great circle paths that intersect both coasts show peaks whenever large waves hit either coast. Thus peaks in the hindcast at either coast will correlate with some but not all of the peaks in the beamformer output at this azimuth, and the CBH at both coasts is diminished. Signal from this region is highest from October–March, consistent with the occurrence of large waves from winter storms (Figure 2d).

[42] Although weaker than the Atlantic signals, high CBH is observed near Alaska (Figure 5a) and the NE United States. The rest of the ocean correlates very poorly with the beamformer output in the NH winter. This is consistent with near-coastal generation of PM signals.

[43] In the SH winter, positive CBH is observed off the coasts of Greenland and Newfoundland, the eastern United states, Polynesia, New Zealand, and Alaska (Figure 5b). Of these, the highest power is observed from the direction of Polynesia. Time series of the beamformer output and the ocean wave hindcasts from this region (pluses in Figure 5b are shown in Figure 5c). The high CBH suggests that large storms generated in the Southern Ocean impart energy in the PM band as their waves pass Polynesian island chain. The PM signal then propagates across the Pacific Ocean to the array.

3.3.3. Double-Frequency Microseisms

[44] During the NH winter, in the frequency band containing the DF peak (0.11–0.13 Hz), the highest CBH occurs near the coastlines of Newfoundland, Greenland and Alaska (Figure 6a). During the SH winter, the highest CBH are observed off the coasts of Newfoundland, Alaska, the eastern coast of the United States, the Pacific coast of Central America, the Alaskan coast and the eastern South Pacific (Figure 6b).

[45] In the eastern North Pacific and western North Atlantic, the highest CBH is observed near the coast. A rigorous analysis of the location of DF sources would require measurements of opposing wave contributions over

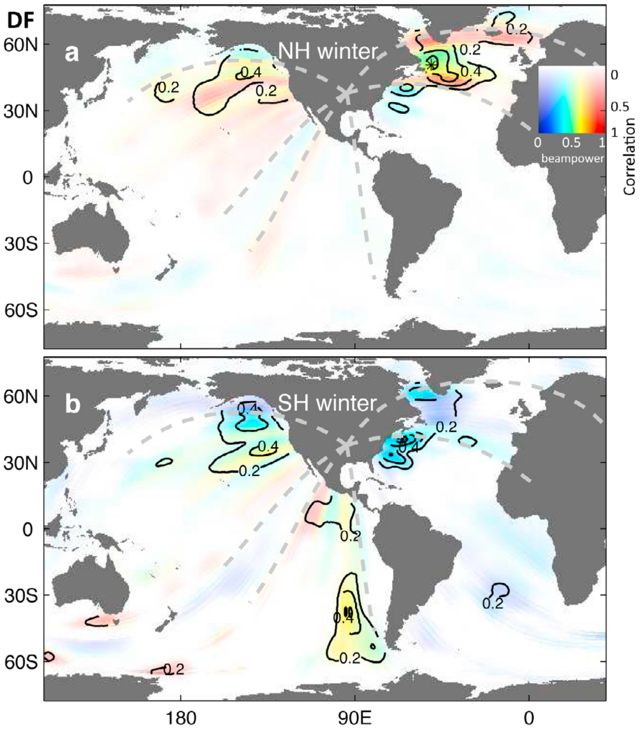

Figure 6. Double-frequency correlations. The same as Figures 4a and 4b with a beamformer output averaged over 0.08–0.16 Hz and 0.24–0.28 s/km. The dashed lines correspond to the azimuths marked in Figures 2g–2i. For the year, the correlation mean, maximum and standard deviation were: $\bar{c} = 3.9 \times 10^{-4}$, $\max(c) = 9.1 \times 10^{-3}$, $\sigma_c = 1.0 \times 10^{-3}$.

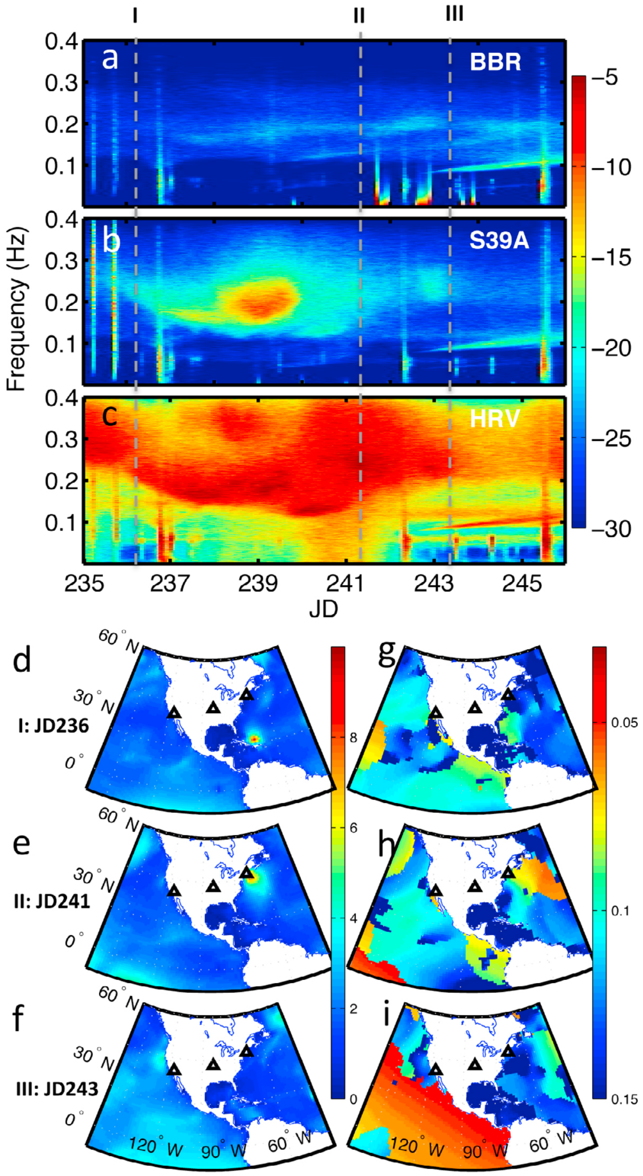

Figure 7. Spectrograms of seismic data from JD235–246 2011 from (a) BBR in California (b) S39A in Missouri and (c) HRV in Massachusetts. Hindcasts of (d–f) significant wave height and (g–i) the frequency of the most powerful wave component. The vertical dashed lines in Figures 7a–7c mark the time periods shown in Figures 7d–7i. Data from the spectrograms are marked as triangles in Figures 7d–7i.

large regions that is unfeasible. Although model wave directional spectrum estimates can be used [*Kedar et al.*, 2008; *Ardhuin et al.*, 2011], these have inherent uncertainties associated with model wind fields used to force the wave models. However, the high correlations obtained here suggest that waves at these coastal locations consistently generate opposing components that cause DF pressure signals. Thus, although wave reflection from coasts is non-linear with frequency [*Elgar et al.*, 1994], an increase in wave height would tend to also generate an increase in opposing wave components, which together will cause an associated increase in DF signal levels. These correlations suggest that, although DF signals can be generated in the deep ocean, some, if not most, of the DF energy measured by the USArray must have been generated in coastal waters.

[46] In both the NH and SH winters, there are azimuths transecting the Pacific with high amplitude DF beamformer output (Figures 2h and 2i) which do not correlate with ocean waves anywhere, except weakly with regions off the coast of Australia and Antarctica (Figure 6). There are a number of possible reasons for the weak correlation: (1) Some azimuths transect multiple coasts, each of which might generate signals at different times. (2) The strong normalization employed distorts the amplitude of beamformer output peaks. This distortion is likely to be exacerbated if many different signals are produced in different locations simultaneously along the same azimuth. (3) The generation of DF microseisms may not be linearly related to ocean wave height because the generation of DF signals requires opposing waves that may not occur. Thus large waves with no opposing waves will generate no DF signal, while small waves interacting with other waves can generate significant DF signal. Relatively small amplitude waves could produce strong DF signals in areas where coastal reflection of wave energy is high.

4. Hurricane Irene

[47] Eleven days of microseism data between 0Z Julian Day (JD) 235 (Aug 23rd) and 0Z JD247 (Sep 4th) 2011 were examined in detail. The data processing differed from section 2 in that the frequency bands were tailored to fit the spectra of the Irene storm waves (Figures 7g–7i and Table 1) and the slowness bins used were 0.04–0.4 s/km. Seismometers in Missouri and Massachusetts Figures 7b and 7c show high amplitude signals between JD234–243, concurrent with the arrival of waves from Hurricane Irene at coastlines.

[48] Hurricane Irene made landfall on the Caribbean islands on JD234 2011. On JD236 (Figures 7d and 7g), hindcast 7 m significant wave heights with a peak period of 11 s (0.09 Hz) impacted the Caribbean islands. As Irene progressed Northward, the wave peak period increased to 15 s (0.07 Hz) by JD241 (Figures 7e and 7h). All three frequency bands in Figure 2 show a signal is observed from 90–130° at the end of August, suggesting that the incidence of Hurricane Irene on the eastern coast of North America was a dominant source of seismic signal in each band during this time (section 4).

[49] Throughout the duration of Hurricane Irene, most of the waves incident on North American coasts during this summer (that were not associated with Irene) had peak periods less than 10 s (Figure 7) and, hence, DF signals less than 5 s (0.2 Hz). Therefore, the band from 0.05–0.1 Hz (10–20 s) is likely dominated by PM signal generated by waves from Irene. Correspondingly, the frequency band from 0.12–0.25 Hz (4–8 s) is likely dominated by Irene DF microseisms. The band from 0.005–0.02 Hz (50–200 s) is dominated by hum, much of which may be excited by infragravity waves resulting from transformation of swell from Irene.

[50] At 6Z JD 238 (Figures 8a–8d) Hurricane Irene makes landfall on continental North America. Beamforming at this time shows hum, PM and DF seismic signals incident from near the region where the largest waves of Hurricane Irene

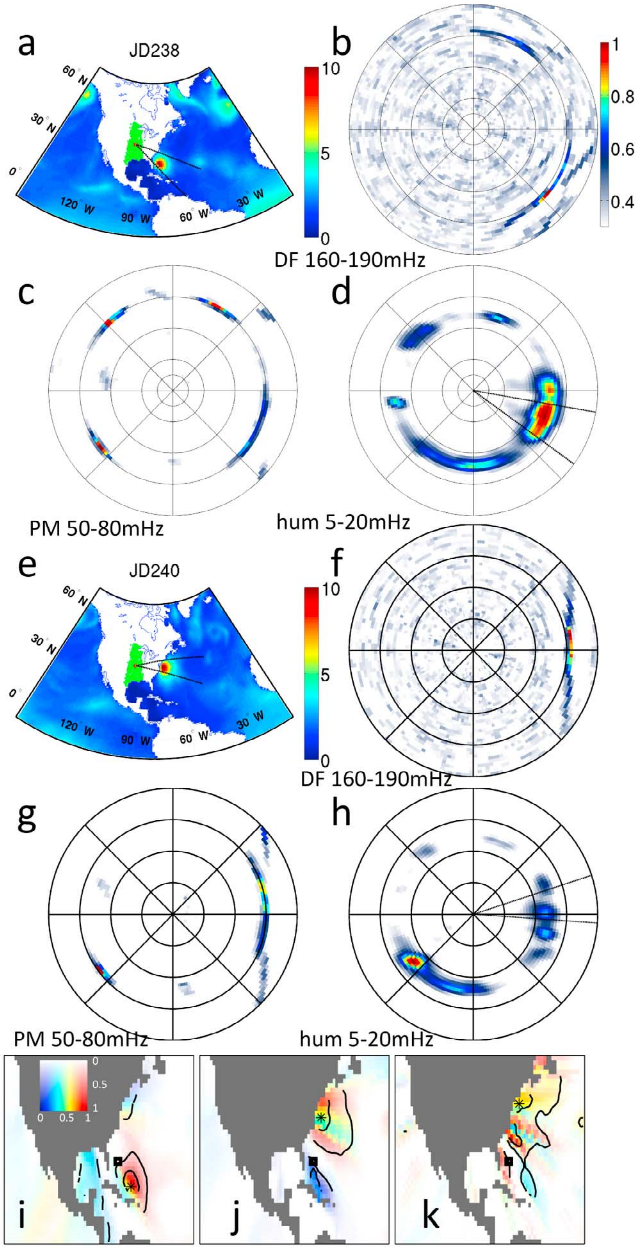

Figure 8. Hurricane Irene. (a) Hindcast of significant wave height from 6Z JD 238 2011. The beamformer output averaged over 5 h for (b) DF, 0.12–0.28, (c) PM, 0.05–0.1 and (d) hum, 0.005–0.02 Hz. The bands have been chosen to isolate PM and DF signals from the peak frequency of waves from Irene (Figure 7h). The beamformer output are plotted radially with slowness 0 s/km at the center and 0.4 s/km at the outer edge. The dashed lines in Figure 8d denote azimuths at which the beam power is 0.75 of the maximum power. The great circle paths associated with these azimuths are plotted in Figure 8a. (e–h) The same as Figures 8a–8d from 9Z JD 240. The CBH from 0Z JD 235–0Z JD 246 for (i) hum, (j) PM, and (k) DF microseisms. The contours show correlations of 0.2 and 0.6. The maximum CBH (asterisk) and the maximal wind strength (square) are indicated.

impact the coast. In the hum and PM bands, other signals are detected from the northwest and northeast resulting from storm waves along the coasts of Alaska and Europe. In the hum band, there is signal incident from the south that may be due to Pacific swell waves incident on the SW coast of Mexico.

[51] At 6Z day 240 (Figures 8e–8h), Hurricane Irene has propagated northward along the eastern coast of North America. Hum, PM and DF signals are continuously spatially and temporally linked with the region where Irene's waves impact the coast. This indicates that the interaction of the hurricane-generated waves with the coastline drives the three seismic generation mechanisms concurrently, and the source regions for microseisms translate northward with the coastal incidence of waves from Irene.

[52] In the hum band there is a prominent signal incident from the southwest, which is larger than the signal from Irene. As the beamforms have been normalized, the presence of this signal may diminish the observed contribution from Irene. Note that the signal from the southwest is larger than that from Irene despite the fact that waves from Irene were larger than waves along the southwest coast of Mexico (Figure 9c).

4.1. Correlation With Ocean Waves

[53] The beamformer output from JD235–247 was correlated with ocean wave hindcasts, selecting only slownesses associated with Rayleigh waves (0.25–0.32 s/km) and smoothing in time (Figures 8i–8k). The PM and DF bands show good correlation of seismic signal with waves in the coastal regions along the east coast (Figures 8j and 8k), likely due to the presence of large waves from Hurricane Irene. For hum, the largest signals and highest correlations are located north of the Caribbean Islands (Figure 8i). Infragravity waves were likely generated on the continental coast, but during this time dominant hum signals were

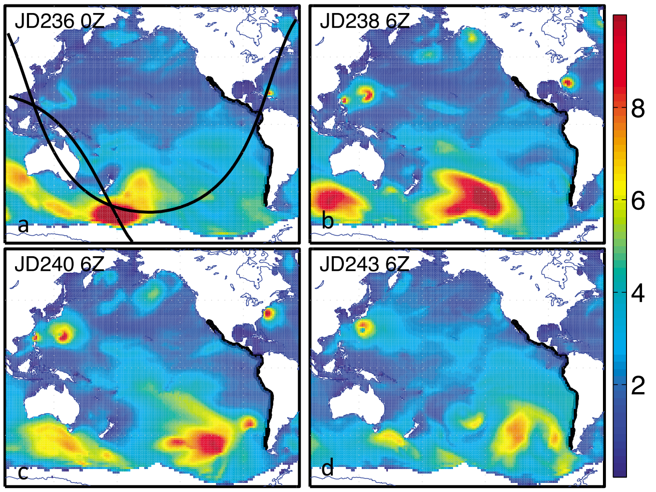

Figure 9. Pacific swell. Hindcasts of significant wave height in the Pacific from (a) JD 236 0Z, (b) 238 6Z, (c) 240 6Z and (d) 243 6Z, 2011. The black lines show the loci 13500 km from the center of the West Coast sub-array and 8610 km from Hawaii. These distances were determined from dispersion trends in Figure 7a and from a seismometer in Hawaii (KIP station, not shown). The coastline along the region illuminated by waves from Southern Ocean storms has been emphasized.

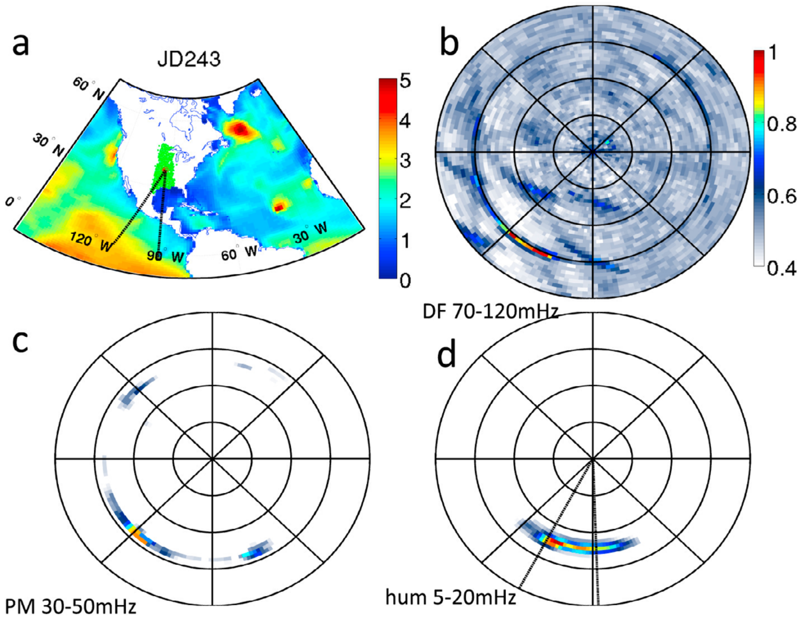

Figure 10. Pacific swell. (a) Hindcast 6Z JD243 2011. The beamformer outputs are plotted radially with slowness 0 s/km at the center and 0.4 s/km at the outer edge for (b) DF, 0.07–0.12 Hz (c) PM, 0.03–0.05 Hz and (d) hum, 0.005–0.02 Hz. The bands have been chosen to isolate PM and DF signals from the peak frequency of waves from the Pacific swell (Figure 7i). The dashed lines in Figure 10b denote the azimuths at which the beam power is 0.75 of the maximum power. The great circle paths associated with these azimuths are plotted in Figure 10a from the center of the array. The beamformer output are averaged over 5 h.

incident from the southwest, which would tend to mask the signal from Hurricane Irene. Hurricane Irene peak wind speeds (square) occur in an area distant from the regions of well-correlated seismic and ocean wave signals, suggesting that factors other than wave height, such as coastal geometry and wave direction, influence the generation of hum and microseisms (section 2.3).

5. Pacific Swell

[54] After Hurricane Irene dissipated, the dominant microseism-inducing wave event affecting North American coasts resulted from a dispersive wave group originating from a Southern Hemisphere storm impinging on the Pacific coast (Figures 7a–7c). All three seismometers shown in Figure 7 show a narrow-band signal that increases linearly in frequency from JD 243–247, consistent with PM microseisms generated by a dispersed wave train. Signals from this wave train are first observed in Hawaii (station KIP, not shown), and subsequently at the other stations a day later. This temporal relationship is consistent with swell propagating east across the Pacific, generating seismic signals when illuminating the Pacific coast of North America, which are detected on the opposite side of the continent.

[55] The gravity wave dispersion relation and the slope of the dispersion trends recorded in Hawaii and California indicate that the waves that generated these signals originated 13500 km from California and 8600 km from Hawaii. Their dispersion also indicates that they were generated 7 days prior to their arrival at the coast of California at 12Z JD242, at a time when the hindcast wavefield shows a large storm in the Southern Ocean at the predicted distance from both California and Hawaii (Figure 9) from frequency-dependent swell propagation speeds. Waves from such Southern Ocean storms are likely responsible for the hum signal observed from the Pacific coasts of Central and South America in Figure 4 [*Bromirski and Gerstoft*, 2009].

[56] These data were beamformed as in section 4 with the filter parameters selected to match the hindcast peak wave period for this wave event (Figure 7i) as shown in Table 1.

[57] Beamforming at 6Z JD243 (Figure 10) shows hum, PM and DF microseisms all incident from the southwest coast of Mexico where the swell waves from the Antarctic storm impact the coast. Hum signals are incident from more southerly directions than the PM signals, which are in turn more southerly than the DF microseisms. This might be due to variations of coastal geometry relative to the incident wavefield, which excite hum, PM and DF energy in different ratios. Or this might be due to attenuation, as the higher frequency signals decay faster and, therefore, appear to be generated at a closer (and, therefore, more westerly) coastline. Thus even if all three signals were generated at constant energy along a stretch of coastline, the closer coastlines could appear to favor higher frequency signals (DF) while the more distant coasts appear to favor lower frequency signals (hum).

[58] Subdividing the USArray into four sub-arrays, beamforming in the hum band on 13Z JD 244 (Figure 11) shows that the dominant hum source region is along the west coast of central Mexico, in agreement with *Bromirski and Gerstoft* [2009]. Even the west coast array detects the dominant hum signal from the southeast rather than the local coast to the west, suggesting that the transformation of swell energy to the infragravity waves that force hum is not uniform along the coast.

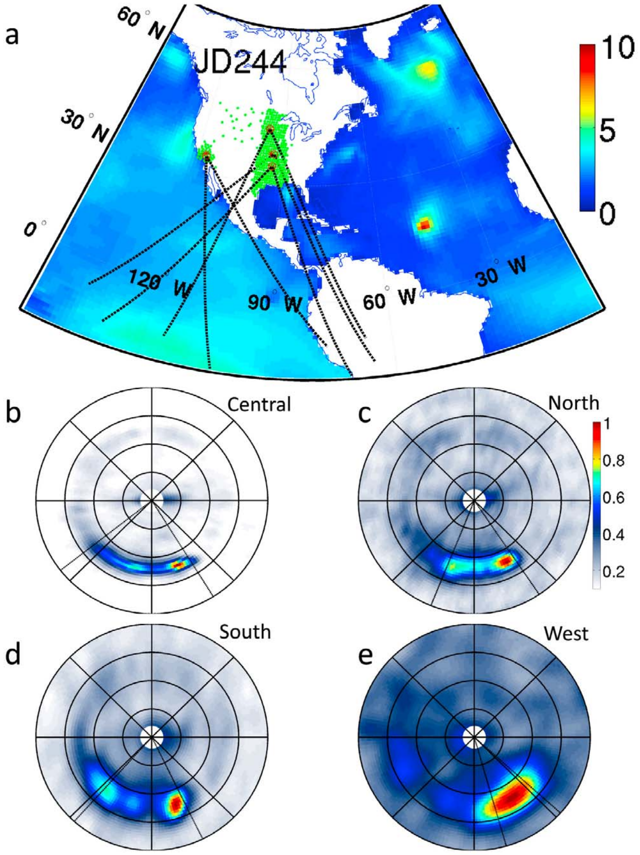

Figure 11. (a) The direction of peak hum incidence for the 4 sub-arrays from 13Z JD 244 2011 overlaid on a hindcast of significant wave height. The beamformer output from a 3-hour average is shown for the (b) Total, (c) North, (d) South and (e) West arrays.

[59] As the significant wave heights are similar across the Pacific coast from Central America to California and larger waves are present in northern California, this suggests that infragravity wave excitation is not linearly related to wave height. Infragravity wave excitation is likely strongly dependent on coastal geometry, the dominant wave period, and the angle of wave incidence to the coast. All the sub-arrays show signals spanning an azimuth range that suggests that the hum signals are generated by a long stretch of coastline. The south sub-array Figure 11d shows three local maxima of the hum signal, indicating multiple regions of coast produce hum simultaneously.

6. Discussion

[60] In the hum and PM bands, the azimuths associated with the largest seismic signals correlate well with coastal waves. Thus the regions of high correlation shown in Figures 4 and 5 are sufficient to account for a significant portion of the wave-generated seismic signals observed by the USArray (Figures 2a–2f). The dominant PM surface wave signals incident from the South Pacific, which the CBH suggests are from Polynesia (Figure 5), have not been reported before. This region is a plausible source of dominant microseisms, as it is regularly impacted by large swell (Figure 3a), however, this requires further study and independent observations to ensure the winter of 2010–2011 was representative, and these results are not due to possible biases in the method (section A2).

[61] High-amplitude signals are observed in the DF band from azimuths that transect the Pacific Ocean (Figures 2g–2i). The CBH along the great circle paths associated with these azimuths correlate weakly near the coasts of Australia and Antarctica (Figure 6). This relatively weak correlation of waves and DF signals observed at the USArray confirms that DF generation is sensitive to factors other than wave height [*Ardhuin et al.*, 2011; *Hillers et al.*, 2012]. This is consistent with DF generation from opposing ocean wave interactions. Moderate amplitude waves interacting with similar amplitude opposing wave components can generate more DF seismic signal than large amplitude waves with small amplitude opposing waves or wave interactions over large versus small areas.

[62] Unlike PM, hum and DF signals can be generated in deep water, and such deep water sources may contribute to hum and DF levels observed on land. However, we have observed hum and DF signals that correlate in time and azimuth with PM signals (Figures 8 and 10), suggesting that the principle coastal PM source regions may also be an important source of hum and DF signals. Prior models of global opposing wave distributions frequently underestimate the DF microseism signal produced in coastal waters [*Hillers et al.*, 2012].

[63] Shallow water DF signal might be due to coastal reflections inducing standing waves, or to evanescent double-frequency oscillations in the water column [*Hasselmann*, 1962]. Non-linear wave interactions of two arbitrary surface-wave components produce second-order surface-wave components with frequencies at both the sum and difference of the first-order wave frequencies. Thus, for an incident wave train with a spread of frequencies, second-order wave components occur at very low frequencies and at double the ocean-wave peak frequency. These components are smaller than the first-order waves and decay exponentially with depth, but they are almost always present and might interact over large areas in near-coastal waters, analogous to the generation of PM signals. Because they do not require the presence of opposing waves, such direct pressure-forced signals might correlate more strongly with wave heights than opposing wave mechanisms.

[64] Only surface wave signals were used in this analysis, as the signals observed by the array showed much more surface wave energy than body waves, suggesting that the body wave DF microseism ocean bottom pressure-to-seismic transfer function is less efficient than that for surface waves. However, beamforming studies with body waves have shown body-wave sources vary seasonally, similar to surface waves. Strong signals were observed in the Southern Ocean during the SH winter, and in the Northern Atlantic and Pacific during the NH winter [*Landès et al.*, 2010].

[65] A detailed examination of two wave events, Hurricane Irene (section 4) and swell from a Southern Ocean storm impacting the Pacific coast of the Americas (section 5), indicates that hum, PM and DF signal are often generated concurrently by waves impacting coasts. For both wave events, seismic signals in all three frequency bands were detected from azimuths that intersected coastal regions

illuminated by the waves. Prior observations of microseism P-wave signals from storm generated waves have shown both temporal correlation between PM and DF bands and dominant generations near coastlines [*Zhang et al.*, 2010].

[66] Compared to other wave-generated seismic signals detected over the year of observation, Hurricane Irene was atypical, and illuminated a region of coastline that does not usually produce dominant microseisms (Figure 2). The Southern Ocean swell event, in contrast, illuminated the coast of South and Central America, which was identified as a region of dominant hum generation throughout the year (Figure 4).

[67] Waves from storms in the Southern Ocean, such as those investigated in section 5, are generated by Southern Hemisphere storms throughout the year, and regularly illuminate multiple coastlines. Swell from these storms impacts the coasts of Polynesia, a region in which PM microseisms correlated well with wave energy (Figure 5). The coasts of southern Australia and Antarctica experience high wave activity throughout the year, with these coasts showing positive CBH with dominant DF beamformer output (Figure 6). Swell from Southern Ocean storms also impact the Americas, a region of dominant hum generation (Figure 4). The waves likely generate seismic signals in all three frequency bands at each coastline, as was shown for the coast of Central America (Figure 10). However, the relative strength of each signal will vary with the wave spectral energy distribution, coastal geometry and the angle of wave incidence, which determines the signal-generation area. The concurrence of these factors caused PM to be the dominant surface wave signal generated at Polynesia, with hum dominant at South and Central America.

[68] Some of the geographic differences observed in the dominant generation regions of the three surface wave bands may be due to attenuation and scattering, both of which generally increase with frequency. Thus the DF beamformer output likely favors identification of generation regions close to the array more so than the hum beamform output. Beamform outputs of wave-generated signals originating along the Pacific coast of the Americas showed the lower frequencies incident from more southerly directions (Figure 10), which implies either a more distant generation region or different wave spectrum characteristics related to storm proximity. Varying coastal geometries and/or attenuation could also be important factors. Attenuation has not been considered here, and thus signals that correlate well with waves at large distances from the array, such as Polynesia in Figure 5, may be underestimated by the beamformer output.

[69] The localization of hum generation regions provides a proxy for remotely identifying dominant coastal infragravity wave source regions. Although the exact relationship between infragravity wave energy at a point in the ocean and the hum source strength is beyond the scope of this work, the extremely long wavelength of infragravity waves indicates they always exert pressure on the seafloor. Assuming that hum signal level scales with infragravity wave energy and that infragravity wave energy is highest in coastal regions [*Herbers et al.*, 1995], the localization of hum generation regions provides a proxy for remotely identifying dominant coastal infragravity wave source regions. Beamformer localizations suggest that strong infragravity waves are produced along the Pacific coast of South America, the northeastern boundary of the Pacific Ocean and, during periods of large swell from storms, the coast of the Iberian peninsula (Figure 4). Additionally, localization of hum sources indicates that secondary infragravity wave generation regions occur along the coasts of New Zealand, South Africa, and the Caribbean and the eastern United States when impacted by hurricanes.

[70] In this work we have only considered the correlation between integrated wave energy distributions (hindcasts) and directional incidence of seismic noise. More information about microseism generation regions could be gleaned by cross-correlating directional microseism power-time series with individual components of 2D wave spectra and, in the case of DF microseisms, with the wave-wave interaction pressure excitation function [*Longuet-Higgins*, 1950; *Kedar et al.*, 2008; *Ardhuin et al.*, 2011]. This could clarify the regional pressure excitation associated with specific wave states rather than seasonally averaged wave states, and presents a logical extension to this work.

7. Conclusions

[71] Cross-correlating beamformed seismic data with ocean wave heights (CBH) identifies regions where ocean wave energy is transformed into seismic surface waves, through interactions with the local seafloor. Prior work has estimated the generation regions of body waves [*Gerstoft et al.*, 2008; *Landès et al.*, 2010; *Zhang et al.*, 2010] and the incident azimuths of surface waves [*Gerstoft and Tanimoto*, 2007; *Bromirski and Gerstoft*, 2009; *Kedar*, 2011]. But there are difficulties in localizing surface wave source regions, as the azimuths intersect large swaths of ocean. When data from multiple arrays are examined, local microseisms will likely dominate beamform outputs from each array. Because the beamform output in this study is normalized across time, there are uncertainties associated with the correlations. However, by averaging over a year, random variations are minimized and the CBH is high only in regions of consistent microseism and hum generation.

[72] Coastal regions generally show higher correlations between seismic surface wave signals and wave height than open ocean regions. This is expected for hum, as the highest amplitude infragravity waves occur nearshore, and for PM, which can only be generated in shallow water. DF microseisms can be generated at any ocean depth. Our correlations indicate that some of the DF microseism energy observed by the USArray was generated in shallow coastal waters, consistent with prior work which showed that when offshore waves were small, coastal waters were a dominant source of DF microseisms [*Hillers et al.*, 2012].

[73] The coastal regions where waves correlate well with seismic surface wave signals vary with frequency band and season. The dominant hum signals are produced along the Pacific coast of Central and South America (SH winter) and the coasts of the North Pacific and Europe (NH winter). The dominant PM signals are produced along the coasts of Polynesia and Alaska (SH winter) and Newfoundland and Greenland (NH winter). Dominant DF signals are produced off the coast of South America (SH winter) and near the east and west coasts of North America (SH and NH winter).

[74] The seismic data recorded during Hurricane Irene and a Pacific swell event indicate that the generation of hum and

microseisms are linked. Beamforming in the three frequency bands (hum, PM and DF) showed signals incident the same directions, and these directions were well correlated with coastal regions impacted by ocean waves. This indicates that ocean swell incident on coastlines produces all three seismic surface wave signals concurrently. Although waves in coastal regions generate all three signals, the distribution of power between these vary with the coastal geometry and the directional spectra of the incident waves. Consequently, the dominant generation regions for each frequency band are different.

[75] Infragravity waves have wavelengths of many kilometers (38 km at 200 s period), and can interact with the seafloor throughout the ocean. The localization of hum generation regions is, therefore, a proxy for global distribution of primary coastal generation regions of infragravity wave energy. These results show that the Pacific coasts of Central and South America are significant source regions of infragravity waves throughout the year.

Appendix A: Data Processing

A1. Detailed Description of Processing Parameters

[76] 1. Filtering: The raw time series for each seismic station, sampled at 1 Hz, was passband filtered in the time domain by a 4th-order Butterworth filter designed to retain signals from hum, PM or DF signals (Table 1):

$$\begin{aligned} y_j^{\mathrm{hum}}(t) &= h_{\mathrm{hum}}(t) * x_j(t) \\ y_j^{\mathrm{PM}}(t) &= h_{\mathrm{PM}}(t) * x_j(t) \\ y_j^{\mathrm{DF}}(t) &= h_{\mathrm{DF}}(t) * x_j(t). \end{aligned} \tag{A1}$$

where $x_j\ (t)$ is the data time series from the vertical motion component of the jth seismic station and h is the passband filter for each component. In the following steps we use the simplified notation $y_j\ (t)$ to represent each component as we perform the same processing for hum, PM and DF components.

[77] 2. Seismic Data Truncation: The time series were split into one-day segments and each day into 200 non-overlapping segments of 432 points. The standard deviation of each segment was computed and the 10 smallest non-zero standard deviations were averaged to give an estimate of the standard deviation of the ambient noise σ_{noise}. Note these segments were used only to estimate the noise standard deviation and are not the same as the segments used in later processing, which are described below. All data points with absolute values greater than σ_{noise} / 2 were set to $\pm\sigma_{noise}$ / 2. This is a low clipping threshold. However, trials with larger thresholds produced beamformer outputs with a large number of transient peaks that evolved on scales too fast to be attributed to ocean waves:

$$\tilde{y}_j(t) = \mathrm{sgn}\left[y_j(t)\right]\frac{\sigma_{noise}}{2}\,\forall\; y_j(t) > \frac{\sigma_{noise}}{2}. \tag{A2}$$

[78] 3. Fourier Transformation: The filtered and truncated time series were downsampled to 0.5 Hz sampling as frequencies above 0.25 Hz contain negligible microseism energy and were excluded from the analysis. The time series were then split into 200 512-point segments (17 min) with an 80-point overlap which were Hanning-windowed and Fourier transformed:

$$Y_j(\omega) = \int w(t)\tilde{y}_j(t)e^{\iota\omega t}\ \mathrm{d}t. \tag{A3}$$

where $w(t)$ is the window function.

[79] 4. Normalization: The snapshots were normalized across frequency bands to reduce high-amplitude narrowband signals. The microseisms are expected to be continuous across the relevant frequency band (Table 1). Thus, any narrowband signal in this range is likely to be a non-microseismic transient:

$$\hat{Y}_j(\omega) = \frac{Y_j(\omega)}{\left|Y_j(\omega)\right|}\quad. \tag{A4}$$

Only the phase of the spectral data vector is retained in $\hat{Y}_j$. Thus, when the data is averaged over stations and frequency during beamforming, the final result is determined by consistent patterns in phase variation across space and frequency, rather than by a small number of high amplitude spectral bins.

[80] 5. Beamforming: Across the array elements (Figure 1), key parameters were aggregated in replica data-vectors that were computed for a range of frequencies, slownesses and azimuths (Table 1). Each replica vector **r** contains the phase relation between the seismic stations for signal from a given azimuth θ, slowness s, and frequency ω, such that the beamformer output

$$B_\theta(s,\omega) = \mathbf{r}(\theta,s,\omega)^H\mathbf{Y}(\omega) \tag{A5}$$

is the summation of the data from each seismic station at frequency ω. $\mathbf{Y}(\omega) = \left[\hat{Y}_1(\omega), \hat{Y}_2(\omega), \ldots\hat{Y}_N(\omega)\right]$ is a vector of the contributions from each of N stations. The replica vector is designed to implement phase shifts to each station such that all components incident with the desired azimuth θ, and slowness s, sum in phase. A different slowness band was used for each frequency band to isolate signals from dispersive Rayleigh waves. All slowness bins spanned 0.01 s/km, and azimuth was sampled from 0–358° using 2° bins. Each replica vector was applied to the data across the array to give a beamformer output as a function of frequency, slowness, azimuth and time.

[81] 6. Averaging: The beamformer outputs were averaged over slowness (see Table 1) and inverse-Fourier transformed:

$$\begin{aligned} \bar{B}_\theta &= \int_{s_{\min}}^{s_{\max}} B_\theta(s,\omega)\ \mathrm{d}s \\ b_\theta(t) &= \textstyle\int \bar{B}_\theta(\omega)e^{\iota\omega t}\dfrac{\mathrm{d}\omega}{2\pi}. \end{aligned} \tag{A6}$$

[82] 7. Beampower Truncation: Despite the clipping applied to transients in the time series (item 2), the beamformer output contained large beampower peaks in single bins (17 min) which have too short a duration to be attributed to ocean waves. All time bins containing values greater than 6 times the mean were replaced with interpolated values from the neighboring bins.

$$b_\theta(t_n) = \frac{[b_\theta(t_{n-1})) + b_\theta(t_{n+1})]}{2}\,\forall\ \max_\theta[b_\theta(t_n)] > 6\bar{b}, \tag{A7}$$

where $\bar{b}$ is the monthly average over time and azimuth, and n is the time index.

[83] 8. Beamformer Output Smoothing: The beamformer output was downsampled from a 17 min to a 3 h sampling interval, using the median value of each 3 h bin.

[84] 9. Normalization: The monthly beamformer outputs were normalized to have a maximum value of one. This allows the beamform power responses from the different frequency bands to be plotted with the same color scale (Figure 2):

$$\tilde{b}_\theta(t) = \frac{b_\theta(t)}{\max_{\theta,t}(b)}. \tag{A8}$$

[85] 10. Interpolation: For each grid point of the hindcast, the azimuth of the great circle path to the array center was computed, and a beampower time series was interpolated for this azimuth. The set of beampower time series were averaged over 6 month periods for the northern (NH) and southern hemisphere (SH) winters (Nov–Apr and May–Oct respectively, Figure 2).

[86] 11. Wave Model Hindcast Smoothing: The hindcast data were median filtered in space across 5 neighboring bins in both zonal and meridional directions. The presence of sea ice was considered a zero in the ocean wave time series. For each grid point, the azimuth to the center of the seismic array was calculated, and a beamformer output interpolated at this azimuth.

[87] 12. Cross-correlation: For each month the hindcast time series and beamform time series at each grid point were cross-correlated, and the value at a time lag of zero gives the *correlation of beamformer output and hindcast* (CBH). The CBH computed for each month were averaged over NH and SH winters. After averaging, the CBH map was normalized to have a maximum value of one:

$$\mathrm{CBH}_k = \frac{\int \left[\tilde{b}_{\theta_k}(t) - \bar{b}_{\theta_k(t)}\right]\left[S_k(t) - \bar{S}_k(t)\right]\mathrm{d}t}{\sqrt{\int \left[\tilde{b}_{\theta_k}(t) - \bar{b}_{\theta_k}(t)\right]^2 \mathrm{d}t}\sqrt{\int \left[S_k(t) - \bar{S}_k(t)\right]^2 \mathrm{d}t}}, \tag{A9}$$

where S_k is the hindcast significant wave height at the kth grid point, θ_k is the azimuth from the array center to the kth grid point, and $(\bar{\cdot})$ denotes the average value over the month.

A2. Interpretation of Correlation With Normalized Beamforms

[88] Due to the normalization across frequency (section A1, step 4) beam amplitudes cannot be compared across time. Rather, each snapshot of the beamformer output is normalized by a different constant. Thus a large beamformer output might not correspond to a large signal. Instead a high value of $\tilde{b}_\theta(t)$, signifies that a large percentage of the energy incident at time t, is incident coherently from azimuth θ. Thus a time series of the beamformer output (Figure 2 and dotted lines in Figures 4 and 5), do not show estimates of the seismic power from this azimuth but the relative contribution of this azimuth to the total power.

[89] The normalization process adds a random component to the beamformer output. However, as the normalization process effectively attenuates the contributions from earthquakes and other transient disturbances, it allows averaging over long time periods. Ensemble averaging over time minimizes this random variation.

[90] Large values of the beamformer output can be related qualitatively to seismic sources. A sudden transient spike in microseism power (see dashed line in Figure 4) indicates that the seismic energy at this azimuth briefly exceeds all other seismic noise sources. The correlation of these spikes with transient spikes in significant wave height suggests that these high-amplitude waves can produce dominant seismic contributions.

[91] Similarly a consistently high beamformer output at an azimuth (see 150–220°, Figure 2a) suggests that sources within these angles are consistently dominant. Thus a consistently high wave height in a region of the ocean corresponding to a consistently high beamformer output suggests these waves correlate with seismic noise.

A3. Interpreting the Correlations From Parallel and Perpendicular Coasts

[92] The coastal geometry relative to the array influences the observed beamformer output and correlation response. Coastlines parallel to the great circle paths may contain a large area of microseism generation observed at the same azimuth. Contributions from coastal waters (Figure 3d) show strong signals at narrow bands at 50°, 160° and 315°, corresponding to the coasts of Newfoundland and Greenland, Central and South America, and the Pacific coasts of North America and Northern Asia. These coasts are parallel to great circle paths from the array. Similar bands are observed in the beamformer output in the hum (50°, 160° and 315°, Figure 2a), PM (50° and 315°, Figure 2d) and DF (50°, Figure 2a) bands.

[93] When computing the correlation, coastlines parallel to great circle paths from the array may underestimate the correlation, as each section may be impacted by waves at different times, each of which is observed at the same azimuth. In this case a beamformer output, containing many events at different times, will be correlated with a series of hindcasts, each of which contains only some of the same events. Thus the CBH will be less than unity. If the waves illuminate the coast perpendicularly, this effect is avoided. Thus, even though the observed beampower in the hum frequency band during the NH winter (Figure 4a) is highest along the coast of South America and the North Pacific coasts (both parallel to great circle paths) the highest CBH is off the Atlantic coast of the Iberian peninsula (perpendicular to great circle paths).

[94] **Acknowledgments.** This work was supported by NSF grants EAR-0710881, EAR-0944109 and OCE-1030022.

References

Ardhuin, F., E. Stutzmann, M. Schimmel, and A. Mangeney (2011), Ocean wave sources of seismic noise, *J. Geophys. Res.*, *116*, C09004, doi:10.1029/2011JC006952.

Ardhuin, F., A. Balanche, E. Stutzmann, and M. Obrebski (2012), From seismic noise to ocean wave parameters: General methods and validation, *J. Geophys. Res.*, *117*, C05002, doi:10.1029/2011JC007449.

Bromirski, P. D. (2001), Vibrations from the “Perfect Storm,” *Geochem. Geophys. Geosyst.*, *2*(7), 1030, doi:10.1029/2000GC000119.

Bromirski, P. D., and F. K. Duennebier (2002), The near-coastal microseism spectrum: Spatial and temporal wave climate relationships, *J. Geophys. Res.*, *107*(B8), 2166, doi:10.1029/2001JB000265.

Bromirski, P. D., and P. Gerstoft (2009), Dominant source regions of the Earth's "hum" are coastal, *Geophys. Res. Lett.*, *36*, L13303, doi:10.1029/2009GL038903.

Bromirski, P. D., and R. A. Stephen (2012), Response of the Ross Ice Shelf to ocean gravity wave forcing, *Ann. Glaciol.*, *53*, 163–172.

Bromirski, P. D., R. E. Flick, and N. Graham (1999), Ocean wave height determined from inland seismometer data: Implications for investigating wave climate changes in the NE Pacific, *J. Geophys. Res.*, *104*(C9), 20,753–20,766, doi:10.1029/1999JC900156.

Bromirski, P. D., F. K. Duennebier, and R. A. Stephen (2005), Mid-ocean microseisms, *Geochem. Geophys. Geosyst.*, *6*, Q04009, doi:10.1029/2004GC000768.

Bromirski, P., O. V. Sergienko, and D. R. MacAyeal (2010), Transoceanic infragravity waves impacting Antarctic ice shelves, *Geophys. Res. Lett.*, *37*, L02502, doi:10.1029/2009GL041488.

Chevrot, S., M. Sylvander, S. Benahmed, C. Ponsolles, J. M. Lefevre, and D. Paradis (2007), Source locations of secondary microseisms in western Europe: Evidence for both coastal and pelagic sources, *J. Geophys. Res.*, *112*, B11301, doi:10.1029/2007JB005059.

Crawford, W. C., S. C. Webb, and J. A. Hildebrand (1991), Seafloor compliance observed by long-period pressure and displacement measurements, *J. Geophys. Res.*, *96*, 16,151–16,160, doi:10.1029/97RG02287.

Duennebier, F. K., R. Lukas, E.-M. Nosal, J. Aucan, and R. A. Weller (2012), Wind, waves, and acoustic background levels at Station ALOHA, *J. Geophys. Res.*, *117*, C03017, doi:10.1029/2011JC007267.

Ekström, G. (2001), Time domain analysis of Earth's long-period background seismic radiation, *J. Geophys. Res.*, *106*, 26,483–26,493, doi:10.1029/2000JB000086.

Elgar, S., T. H. C. Herbers, and R. T. Guza (1994), Reflection of ocean surface gravity waves from a natural beach, *J. Phys. Oceanogr.*, *24*, 1503–1511.

Froment, B., M. Campillo, P. Roux, P. Gouedard, A. Verdel, and R. L. Weaver (2010), Estimation of the effect of non-isotropically distributed energy on the apparent arrival time in correlations, *Geophysics*, *75*(5), SA85, doi:10.1190/1.3483102.

Fukao, Y., K. Nishida, and N. Kobayashi (2010), Seafloor topography, ocean infragravity waves, and background Love and Rayleigh waves, *J. Geophys. Res.*, *115*, B04302, doi:10.1029/2009JB006678.

Gerstoft, P., and T. Tanimoto (2007), A year of microseisms in southern California, *Geophys. Res. Lett.*, *34*, L20304, doi:10.1029/2007GL031091.

Gerstoft, P., P. M. Shearer, N. Harmon, and J. Zhang (2008), Global P, PP, and PKP microseisms observed from distant storms, *Geophys. Res. Lett.*, *35*, L23306, doi:10.1029/2008GL036111.

Guza, R. T., and R. E. Davis (1974), Excitation of edge waves by waves incident on a beach, *J. Geophys. Res.*, *79*(9), 1285–1291, doi:10.1029/JC079i009p01285.

Hanafin, J., et al. (2012), Phenomenal sea states and swell radiation: A comprehensive analysis of the 12–16 February 2011 North Atlantic storms, *Bull. Am. Meteorol. Soc.*, in press.

Harmon, N., C. Rychert, and G. Gerstoft (2010), Distribution of noise sources for seismic interferometry, *Geophys. J. Int.*, *183*, 1470–1484, doi:10.1111/j.1365-246X.2010.04802.x.

Hasselmann, K. (1962), On the non-linear energy transfer in a gravity-wave spectrum, 1. General theory, *J. Fluid. Mech.*, *12*, 481–500.

Hasselmann, K. (1963), A statistical analysis of the generation of microseisms, *Rev. Geophys.*, *1*, 177–210.

Herbers, T. H. C., S. Elgar, and R. T. Guza (1995), Generation and propagation of infragravity waves, *J. Geophys. Res.*, *100*, 24,863–24,872.

Hillers, G., N. Graham, M. Campillo, S. Kedar, M. Landès, and N. Shapiro (2012), Global oceanic microseism sources as seen by seismic arrays and predicted by wave action models, *Geochem. Geophys. Geosyst.*, *13*, Q01021, doi:10.1029/2011GC003875.

Holman, R. A., and A. J. Bowen (1984), Longshore structure of infragravity wave motions, *J. Geophys. Res.*, *89*, 6446–6452.

Kedar, S. (2011), Source distribution of ocean microseisms and implications for time dependent noise tomography, *C. R. Geosci.*, *343*, 548–557, doi:10.1016/j.crte.2011.04.005.

Kedar, S., M. Longuet-Higgins, F. Webb, N. Graham, R. Clayton, and C. Jones (2008), The origin of deep ocean microseisms in the North Atlantic Ocean, *Proc. R. Soc. A*, *464*, 777–793, doi:10.1098/rspa.2007.0277.

LaCoss, R. T., E. J. Kelly, and M. N. Toksöz (1969), Estimation of seismic noise using arrays, *Geophysics*, *34*, 21–38.

Landès, M., F. Hubans, N. M. Shapiro, A. Paul, and M. Campillo (2010), Origin of deep ocean microseisms by using teleseismic body waves, *J. Geophys. Res.*, *115*, B05302, doi:10.1029/2009JB006918.

Lippmann, T. C., R. A. Holman, and A. J. Bowen (1997), Generation of edge waves in shallow water, *J. Geophys. Res.*, *102*, 8663–8679.

Longuet-Higgins, M. S. (1950), A theory of the origin of microseisms, *Philos. Trans. R. Soc. London*, *243*, 1–35.

McWilliams, J. C., J. M. Restrepo, and E. M. Lane (2004), An asymptotic theory for the interaction of waves and currents in coastal waters, *J. Fluid Mech.*, *511*, 135–178.

Nishida, K., and N. Kobayashi (1999), Statistical features of Earth's continuous free oscillations, *J. Geophys. Res.*, *104*, 28,741–28,750, doi:10.1029/1999JB900286.

Nishida, K., N. Kobayashi, and Y. Fukao (2000), Resonant oscillations between the solid earth and the atmosphere, *Science*, *287*, 2244–2246, doi:10.1126/science.287.5461.2244.

Nishida, K., J. Montagner, and H. Kawatsu (2009), Global surface wave tomography using seismic hum, *Science*, *326*, 112, doi:10.1126/science.1176389.

Rhie, J., and B. Romanowicz (2004), Excitation of Earth's continuous free oscillations by atmosphere-ocean-seafloor coupling, *Nature*, *431*, 552–556, doi:10.1038/nature02942.

Rhie, J., and B. Romanowicz (2006), A study of the relation between ocean storms and the Earth's hum, *Geochem. Geophys. Geosyst.*, *7*, Q10004, doi:10.1029/2006GC001274.

Schimmel, M., E. Stutzmann, F. Ardhuin, and J. Gallart (2011), Polarized Earth's ambient microseismic noise, *Geochem. Geophys. Geosyst.*, *12*, Q07014, doi:10.1029/2011GC003661.

Stroeve, J. C., J. A. Maslanik, M. C. Serreze, I. Rigor, W. Meier, and C. Fowler (2011), Sea ice response to an extreme negative phase of the Arctic Oscillation during winter 2009/2010, *Geophys. Res. Lett.*, *38*, L02502, doi:10.1029/2010GL045662.

Stutzmann, E., M. Schimmel, G. Patau, and A. Maggi (2009), Global climate imprint on seismic noise, *Geochem. Geophys. Geosyst.*, *10*, Q11004, doi:10.1029/2009GC002619.

Svendsen, I. A. (2006), *Introduction to Nearshore Hydrodynamics*, chap. 14, pp. 661–673, World Sci., Singapore.

Tanimoto, T. (2008), The oceanic excitation hypothesis for the continuous oscillations of the Earth, *Geophys. J. Int.*, *160*, 276–288, doi:10.1111/j.1365-246X.2004.02484.x.

Thomson, J., S. Elgar, and T. H. C. Herbers (2005), Reflection and tunneling of ocean waves observed at a submarine canyon, *Geophys. Res. Lett.*, *32*, L10602, doi:10.1029/2005GL022834.

Thomson, J., S. Elgar, B. Raubenheimer, T. H. C. Herbers, and R. T. Guza (2006), Tidal modulation of infragravity waves via nonlinear energy losses in the surfzone, *Geophys. Res. Lett.*, *30*, L05601, doi:10.1029/2005GL025514.

Tolman, H. L. (2005), Manual and wave user system documentation of WAVEWATCH-III version 2.22, U.S. Dep. of Commer., Washington, D. C.

Uchiyama, Y., and J. C. McWilliams (2008), Infragravity waves in the deep ocean: Generation, propagation, and seismic hum excitation, *J. Geophys. Res.*, *113*, C07029, doi:10.1029/2007JC004562.

Weaver, R. L., B. Froment, and M. Campillo (2009), On the correlation of non-isotropically distributed ballistic scalar diffuse waves, *J. Acoust. Soc. Am.*, *126*(4), 1817–1826, doi:10.1121/1.3203359.

Webb, S. C. (2007), The Earth's 'hum' is driven by ocean waves over the continental shelves, *Nature*, *445*, 754–756, doi:10.1038/nature05536.

Webb, S. C. (2008), The Earth's hum: The excitation of Earth normal modes by ocean waves, *Geophys. J. Int.*, *174*, 542–566, doi:10.1111/j.1365-246X.2008.03801.x.

Zhang, J., P. Gerstoft, and P. D. Bromirski (2010), Pelagic and coastal sources of P-wave microseisms: Generation under tropical cyclones, *Geophys. Res. Lett.*, *37*, L15301, doi:10.1029/2010GL044288.